Terr. Atmos. Ocean. Sci., Vol. 31, No. 6, 663-675, December 2020 doi: 10.3319/TAO.2020.04.02.01

Establish an efficient method to monitor slope deformation using PS-InSAR, MUAV, and surveillance cameras

Chia-Sheng Hsieh * and Di-Yi Lin

Department of Civil Engineering, National Kaohsiung University of Science and Technology, Kaohsiung City, Taiwan

Article history:

Received 28 July 2019
Revised 30 March 2020
Accepted 2 April 2020

Keywords:

Surface deformation, PS-InSAR, MUAV, Surveillance camera, Hierarchical monitoring procedure

Citation:

Hsieh, C.-S. and D.-Y. Lin, 2020: Establish an efficient method to monitor slope deformation using PS-InSAR, MUAV, and surveillance cameras. Terr. Atmos. Ocean. Sci., 31, 663-675, doi: 10.3319/TAO.2020.04.02.01

ABSTRACT

The Taiwan area of mostly rugged mountains and special geological conditions induced catastrophic slope deformation by heavy rainfall and earthquakes. Unstable hillslopes present a significant problem especially to buildings because it affects the living safety. This article mainly discusses regions with buildings in a wide hillslope and proposes a set of hierarchical monitoring procedure. First, persistent scatters interferometric synthetic aperture radar (PS-InSAR) technology observes a wide region of displacement by SAR images, hence detects result of severe displacement regions as the interested areas. Furthermore, multi-rotors UAV (MUAV) captures high-resolution images calculation deformation in the interested areas, which evaluates the serious displacement as a high-risk region. Finally, the self-develop surveillance cameras monitoring system achieves real-time displacement and behavior in the high-risk regions. The study area is located in the campus. From the hierarchical monitoring procedure results, PS-InSAR investigation in the large region is found to be reliable and reasonable, which can provide MUAV flight an effective reference. Both the PS-InSAR and MUAV showed a ground maximum displacement of 30 mm yr^{-1} (LOS velocity) in the interested areas where ground displacement is higher than the building. The advantages of surveillance cameras include obtaining real-time displacement and providing clear surface erosion behavior. This study experimentally demonstrated and provided a reliable hierarchical monitoring procedure and deformation information of different scales through three remote-sensing techniques.

1. INTRODUCTION

Taiwan is situated at ample rainfall position and at a junction of seismic plates. Furthermore, two-thirds of Taiwanese topography consisted of hillslopes. All these factors induced hillslope deformation, particularly when faced with extreme climate events, such as Caoling, Jioufenershan, and Hsien-du-shan in the upstream of the village Xiaoling; 115.9-k of Suhua highway; the Qidu section of the National freeway No. 3; and Lidao to Wulu section of the Southern Cross-Island highway. It must be noted that the historical events of severe deformation can reflect residential environment safety.

In general, regular data has emerged as important information for monitoring and measuring the displacement of large region. Results signify the need to plan a more detailed evaluations deformation trend. Most especially, severely deformation areas utilize real-time tool in order to increase the dense time of the observations. Therefore, proper investigation, evaluation, and measurement of hillslopes can be considered as an efficient monitoring method.

Consequently, large region monitoring are commonly employed for SAR images. Fixed orbit and period of satellites, also contribute in the investigation of surface deformation with a time series. Based on the SAR images, various technologies have been developed and applied (Ferretti et al. 2000; Hilley et al. 2004; Hooper et al. 2004), such as conventional differential synthetic aperture radar interferometry (DInSAR) or persistent scatters interferometric synthetic aperture radar (PS-InSAR). On the other hand, multi-rotors UAV (MUAV) can collect high-resolution images in specific areas, which is classified as a quickly observed and highly maneuverability tool. The MUAV image commonly

* *Corresponding author*
E-mail: hsieh@nkust.edu.tw

adopted photogrammetric technology techniques for obtaining digital surface model (DSM) and orthophotos, which can be used to calculate surface deformation with multi-period. High-resolution orthophotos can be applied to determine the horizontal deformation (Fernández et al. 2015) and to analyze the deformed trend of gap (Stumpf et al. 2013). DEM can be used to calculate volume of deformation (Niethammer et al. 2010, 2011), and the deformed trends (Carvajal et al. 2011). This also provides DEM of each period to register precise position, which could auto detect the region and direction of displacement (Niethammer et al. 2012). Therefore, MUAV has been used to monitor slope deformation as a measure for disaster management.

In most of the previous studies, SAR and MUAV images regularly provide deformation region and location, which is a key advantage of both methods. However, the certainty of deformation is often difficult to evaluate due to the lack of real-time data processes before the disaster. Therefore, many studies use a single surveillance camera to examine the situation of an area online (Akca 2013; Ide and Oguma 2013).

This study first used long-term PS-InSAR techniques to obtain deformation in a wide region, which selected a serious deformation area around buildings as an interested area. High-resolution of MUAV images are adopted to evaluate short-term deformation trends. From the information above, the high-risk region is determined, which can be focused and monitored in real-time using surveillance cameras.

Therefore, based on the advantages of PS-InSAR, MUAV, and surveillance cameras, this study establishes a set of investigation, evaluation, and real-time hierarchical monitoring procedure applied to hillslopes. This kind of data demonstrates an economic and timely way of using remote-sensing-based hazard mitigation and risk analyses.

2. STUDY AREA

In general, earthquakes and heavy rain had caused landslides (Nadim et al. 2006; Pesci et al. 2011). The study area is located in Yanchao campus of National Kaohsiung University of Science and Technology (NKUST), which belongs to Yanchao District, Kaohsiung County, Taiwan (Fig. 1). Its geology is composed mainly of mudstone (Lu 2014), and the region was struck by the massive rainfall brought by Typhoon MEGI in 2016, which caused severe geological hazards and buried three lives (Chang 2018) near the study area, which geologically consisted of mudstone.

Geologic reports (NKUST 2009) show that the surface is composed of weathered mudstone and more sensitive deeper mudstones, which was formed rapidly that soften and disintegrate upon contact with water. The Central Weather Bureau showed that the accumulated rainfall has an average of 1885 mm at the Kaohsiung station during 1981 - 2010 (Central Weather Bureau of Taiwan 2020). The rainfall is abundant but the distribution is uneven. The distribution concentrates in May to September, which accounts for more than 90% of the annual rainfall. The study area's average slope is 27 degrees and the hillslope surface has been artificially excavated. Thus, the above hazard factors constitute an unsafe situation.

3. METHODOLOGIES

To effectively monitor a wide study area, this study proposes a monitoring procedure. First, the hierarchical procedure investigates a large region, which can select serious deformation area around buildings as the area of interest. Short-term deformation trends in the interested area are evaluated as a high-risk region. Finally, a real-time method

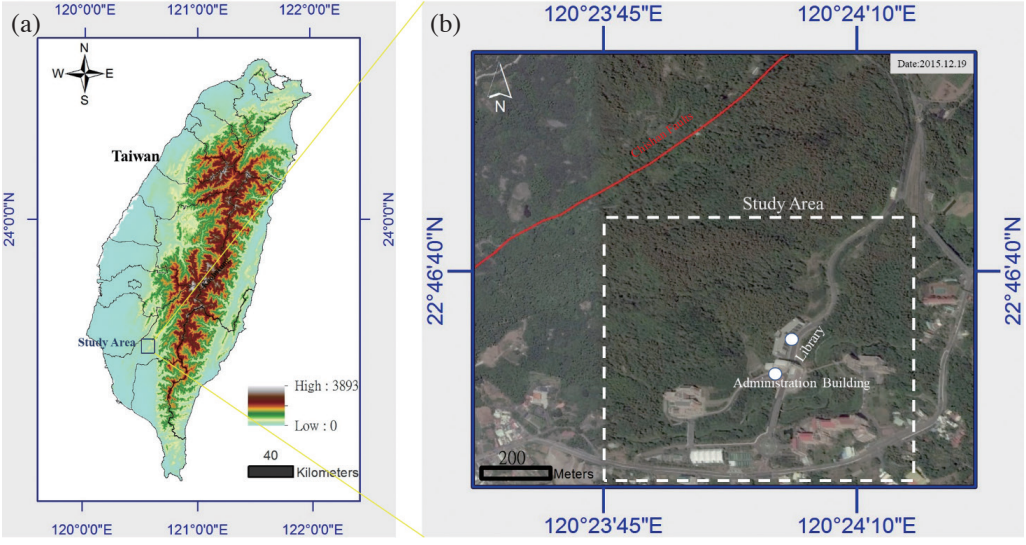

Fig. 1. Location of study area (a) located in the Yanchao District, Kaohsiung, Taiwan and (b) the area of Yanchao campus, NKUST.

is used to focus and monitor the high-risk region. The different steps required above complete the hierarchical monitoring procedure.

3.1 PS-InSAR

SAR images are selected to investigate the deformation for a wide area. SAR images have the advantages of repeated observations, all-weather situations, and large-area measurements. The commonly used frequencies for SAR images are the X-band (12.5 - 8 GHz, 2.4 - 3.75 cm wavelength), C-band (8 - 4 GHz, 3.75 - 7.5 cm wavelength), and L-band (2 - 1 GHz, 15 - 30 cm wavelength) (Lillesand et al. 2008). However, different satellites have different scanning frequencies. To overcome these limitations, InSAR-based information can be enhanced through multi-temporal interferometric techniques (MIT), based on the analysis of long stacks of co-registered SAR imagery (Ferretti et al. 2001; Crosetto et al. 2016). In the past years, several MIT approaches have been developed such as the permanent scatterers interferometry, named PS-InSAR™ (Ferretti et al. 2000, 2001; Colesanti et al. 2003) and the Stanford method for persistent scatterers StaMPS (Hooper et al. 2004, 2007). This study selected StaMPS to process SAR images to obtain PS (persistent scatterers) points.

PS-InSAR extends from the InSAR technique. The scatterers with better character and stability will be chosen as PS such as for building corners, bridges, roads, or exposed rocks. It can provide higher radar echo signal and reliable phase value. With these differences of PS, we could estimate the deformation for satellite direction at different times. Since the radar images are acquired in a wide region (100 km^2) scanning, the results calculated by PS-InSAR could exhibit a lot of PS. PS-InSAR is a technology with high space density, high accuracy, and low cost. Taiwan has many slopes but most are covered by vegetation. To achieve better result, the study chose to use the L-band advanced land observing satellite (ALOS, ALOS-2) and the C-band Sentinel-1 satellite to quickly detect the surface deformation of the study area by PS-InSAR.

The PS point can provide a variation of the stable region (buildings, roads, rocks), but the change of the stable region needs to be slowly moving (Righini et al. 2012). The advantage of PS is that it can accurately calculate the time series analysis of slope deformation and determine the speed of slope sliding (Berti et al. 2013). Taiwan-related research utilized PS to collect surface deformation, such as Huang et al. (2016a) who reviewed 15 years of surface deformation in Western Taiwan with insight from SAR interferometry. Utilizing the same surveying technique, Huang et al. (2016b) studied multiple fault slip triggered above the 2016 M_w 6.4 MeiNong earthquake. Du et al. (2017) tracked landslide movement of time series in Tsaoling. Shih et al. (2019) monitored a landslide of vegetated area in Liugui.

In addition, the SAR images imaging process is a slant range image, such as the 5 - 20 m (Interferometric Wide Swath Mode) resolution of the Sentinel-1 satellite. Therefore, SAR images are used to investigate the results of large-scale areas which can assess the interested area, providing a good flight region reference for MUAV.

3.2 MUAV

MUAV acquires image with advantages of convenient flying preparation and high resolution. Structure from motion (SFM) algorithm is one of the commonly adopted techniques for obtaining point cloud, interior, and exterior orientation, which can be used to generate DSM and an orthophoto (Vasuki et al. 2014). SFM algorithm has been verified to accurately obtain 3D terrain information (Mancini et al. 2013; Turner et al. 2015; Fernández et al. 2016).

The higher the image resolution, the better the accuracy of the SFM algorithm (James and Robson 2012). Hsieh et al. (2016) estimated DSM and error by aerial photogrammetry, airborne LiDAR, and UAV for estimation. Cook (2017) evaluated the effectiveness of low-cost UAVs and structure from motion for geomorphic change detection. For other types of research, Deffontaines et al. (2017) used to analyze interseismic shallow deformation of the Pingting terraces with both UAV and PS-InSAR. Deffontaines et al. (2018) also utilized the same surveying technique that studied onshore Hengchun Fault.

However, it produces an increase in resolution cause by cost increase. The cost is then balanced by satisfying the flight region supply and demand with the help of the interested area. Moreover, both the stable and unstable areas can calculate displacement and volume, as well as high-risk region assessed in the interested area.

In addition, the MUAV has difficulty acquiring images of high-risk region in strong winds and rainy days, which can be used after the disaster. To immediately understand actual scene, commercially available surveillance cameras are selected.

3.3 Real-Time Surveillance Cameras

The surveillance camera has a real-time image transmission function that can be considered as a tool for quickly achieving the current scenes. Some surveillance cameras have a waterproof function, enabling it be set outdoors.

Therefore, this study is able to propose a system of multiple surveillance cameras (Lin et al. 2017), which focus real-time at high-risk region. Moreover, the images of each camera need to overlap. The network service makes streaming live from remote locations and synchronous capture images possible. Live image in each period generates 3D point clouds by the SFM algorithm. The above description surveillance system is shown in Fig. 2. The surveillance

camera collects high-resolution image at a limiting distance, when high-risk region is focused. It must be noted that pixel size is used to determine which distance can be considered as accurate. Therefore, selection of the high-risk region is very important.

The point cloud per period uses the Hausdorff distance method to calculate deformation (Huttenlocher et al. 1992). This study assumes that the deformation of the soil is the shortest distance change, and the variation can be divided into three axial directions as the soil movement.

4. RESULTS AND ANALYSIS

4.1 PS-InSAR

This study first selected ALOS-1 PALSAR SAR images, from 2007/01/17 to 2011/03/15 with a total of 15 images, over a period of 4 years. PS-InSAR algorithms use a single master stack. This is why the study selects the 2009/10/25 SAR image as a master. PS results are then generated as shown in Fig. 3.

Figure 3a shows that the PS points are distributed densely and PS points are also acquired in forest areas. L-band (ALOS-1 PALSAR) SAR images can penetrate into the vegetation area and assess the deformation and behavior of vegetation-covered region, which is important for monitoring key. Therefore, the study uses ALOS-1 PALSAR SAR images, which can be obtain PS for vegetation-covered region in the study area. In Fig. 3, the warm color indicates that the surface deformation is close to the satellite direction, and the cool color indicates that the surface deformation is far away from the satellite direction. In the study site 91 PS points are shown in Fig. 3b, that the maximum Line of Sight (LOS) deformation rate is 15.8 mm yr^{-1}.

The ALOS-1 PALSAR SAR images are monitoring results by 2012 but built some buildings that are completed in 2015. They may have sabotaged the slope and change the original behavior of deformation. To monitor deformation after the new facility, the selected Sentinel-1A ascending images (2015/06/19 - 2016/07/07) and descending images (2015/06/09 - 2016/07/21), are employed using the same

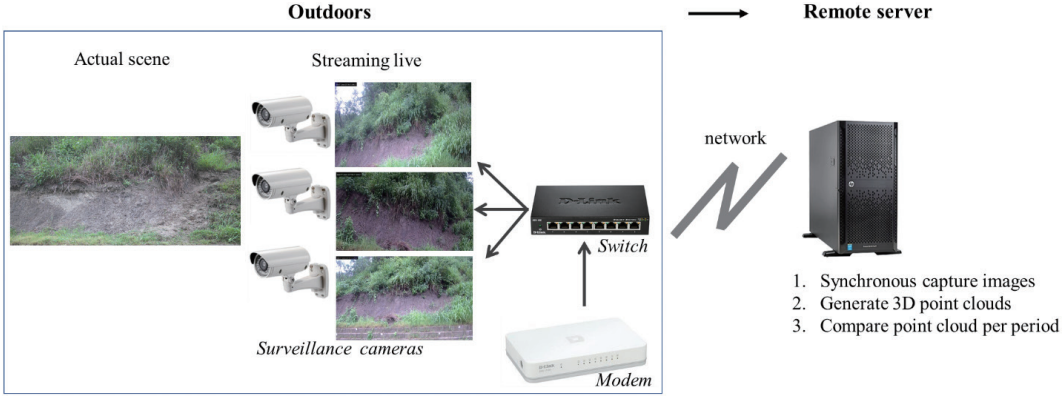

Fig. 2. Self-developed surveillance cameras system in operation.

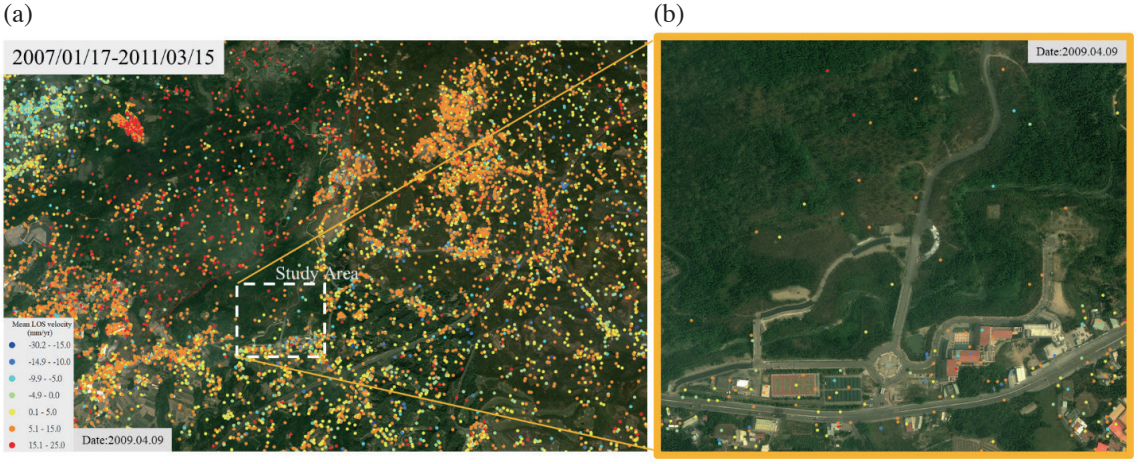

Fig. 3. Result of PS-InSAR by ALOS-1 PALSAR SAR images (2007/01/17 - 2011/03/15). (a) PS point of Yanchao District, Kaohsiung, Taiwan and (b) yellow square is the area of interest in the study area.

PS-InSAR technique. PS points are then generated, and the result is shown in Fig. 4.

Figure 4 shows that the PS point is quite dense in the building area, but there exists fewer PS points in the forest area. Because the Sentinel-1 satellite SAR image is C-band, it is more difficult to produce PS points for vegetation-covered region. In Fig. 4, the warm color indicates that the surface deformation is close to the satellite direction, and the cool color indicates that the surface deformation is away from the satellite direction.

As show in Figs. 4a and b, the distribution of PS points around the study area clearly observes different displacements on both sides of the Chishan fault. PS point with 23.3 mm yr^{-1} change max rate is located at the south side of the Chishan fault, so study area clearly has displacement. In addition, the study area displacements separately exhibits a change rate of -1 to 9 mm yr^{-1} for ascending images and -16 to -1 mm yr^{-1} change rate for descending images. Ascending and descending areas are the angle and azimuth of different directions. From the acquired images, that are observed by different satellite LOS value located in the southwest part of Taiwan, it is displaced about 60 mm yr^{-1} to the southwest (Ching et al. 2016). Finally, we adopt Taiwan's continuous GPS stations SG77 to analyze PS points accuracy. SG77 position information of total displacement is 15 mm during 2015/06 - 2016/07. This position separates result into an LOS value of 5.6 mm (ascending) and LOS value of 7.9 mm (descending) in Fig. 4. LOS result of accuracy is 0.9 and 1.4 mm for ascending and descending, respectively.

PS points can provide a valuable deformation trend. To evaluate maximum displacement region between the three kinds of PS points, we used the natural neighbor interpolation algorithm to raster. Natural breaks classification methods (Jenks 1963) are then utilized to divide into classes whose boundaries are set where there are relatively big differences in the data values, as show in Fig. 5.

This ALOS-1 PALSAR SAR image analysis showed a displacement in the dormitory surrounding of 9.1 mm yr^{-1}, which is the maximum displacement rate in one figure (Fig. 5a). However, some buildings are already completed such as the library and the administration buildings in 2015. Therefore, Sentinel-1A SAR images (ascending and descending) are adopted. Comparing their results (Figs. 5b, c), a very similar information of maximum displacement is yielded in the library surrounding of the smaller study area. Finally, we can investigate the library surrounding as the maximum displacement. The interested area is calculated according to the building foundation of quadruple depth (32 m), which is 8 m of the library foundation depth, as seen in Fig. 5. The interested range according to Peck (1969) suggests an excavation disturbed region, which was double to quadruple foundation depth. Furthermore, Sentinel SAR image time span and interested area, which is a reference of the MUAV.

4.2 MUAV

A self-made 4-rotor MUAV platform by 75-cm length is made and equipped with autonomous aircraft, GPS, and a 6-S 12000-mAh battery, which can achieve 25 flight time. The camera is a Canon EOS M camera with an EF-M 22 mm f/2 STM prime lens, which can be set with 2-axis tripod head system, as shown in Fig. 6. Its image size is 5184 × 3456 pixels. The flight height is 100 m with 2 cm ground sampling distance and coverage of the adjacent photos is kept at least for 90% overlap and 60% sidelap. The interested area needs a total of eight air routes, yielding about 253 images per flight, which completes the task in 13 minutes.

To evaluate the surface deformation in the interested area, MUAV images are collected on 2015/06/02 and 2016/06/23 according to Sentinel SAR image date. The datasets generated in this study are the orthophoto and DSM with a grid spacing of 2 cm, as shown in Fig. 7. To get these results, the MUAV images were processed by Agisoft PhotoScan software. Orthophoto shows that the slope at the back of the administration building and library is covered by lush vegetation, and there is little short vegetation on the irregular bare soil area above the detention pond. DSM shows that the difference of elevation is 91 m. Finally, ground control points (GCPs) horizontal and vertical accuracies are checked to be 2.0 and 3.2 cm, with located position as shown in Fig. 7.

To understand the deformation in this area of interest, we first remove the lush vegetation region and then use two DSMs to quantify surface change. Therefore, we performed a period of DSMs comparisons, which can be calculated as the surface amount of deformation (see Fig. 8). Based on the result analyses activity of deformation, we discover susceptible A and B zones. A zone is a visibly deposed zone with stack height of about 0.1 - 2.0 m, while the B zone can be assigned to erosion and deposition components and exhibits an average of 0.39-m deformation with closed buildings.

Furthermore, the B zone is bare soil with a slope average of 58 degree and slope toe region. According to the above factors that can be considered very sensitive deformation area, slope protection works were completed on 2017/04. Therefore, this has an unstable condition. The mean deformation trend reflects more probability of severe deformation, such as erosion throughout the slope toe, which may affect safety of building. Indeed, soil is slowly disappearing inside the B zone during monsoon seasons. This is considered as a high-risk region.

4.3 Real-Time Surveillance Cameras

The high-risk region in Fig. 9 shows the B zone of about 8 m wide and 6 m high, where attention is focused. Thus, a real-time monitoring system is achieved in this case. According to systems requirements (Lin et al. 2017), a total of three surveillance cameras, separated by 80 cm (90%

overlap) with photographic distance from 2.4 to 4.4 m are needed. Figure 9 shows the actual site. This system developed the tool by Python for capturing synchronous images and generating dense point clouds. The whole procedure can be completed in 10 s to each period. Because the image from surveillance cameras are not associated with any position information, GCPs are required for relative accuracy. Six GCPs are created on the fence because this position belongs to a stable facility in the image view, which can check accuracy to each period. Evaluation results show that the average horizontal and depth accuracies are 0.9 and 1.2 cm, respectively. This system started to operate in 2017/05. Furthermore, surface property assigned C zone of fine particles and D zone of sticky particles in high-risk region.

One period, 2017/06/04 exhibits a rainfall of 77 mm. Therefore, the surveillance cameras collect images from 7 a.m. to 5 p.m., for a total of 10 hours. Figure 10 shows the elevation deformation at some important time. D zone starts to change at 7:15 a.m. and then C zone appeared deformed 10 minutes later, C zone and D zone generate visible deformation at 12:40 a.m. and 1:50 p.m. respectively. Both zones stop changing at 4:45 p.m. Each period proceeded as described in the methods above, showing that the serious period happen at around 1:00 - 2:00 p.m., which reveals the heavy rainfall during this period.

5. DEFORMATION ANALYSIS

5.1 PS-InSAR and MUAV of Deformation Analysis

A complete hierarchical monitoring procedure is provided that separates different surface deformation condition, which can then be evaluated as high-risk region. In region established based on PS-InSAR and UAV image technology, we explore two different remote-sensing techniques to observe deformation trends. Both can have a mutual assistance to analyze deformation behavior since they have been developed for the different surface deformation characteristic.

Based on the experiment conducted from Sentinel-1A SAR images in the interested area (Fig. 11), 14 PS points of ascending image, 16 PS points of descending image, and PS points of 10-m resolution overlay MUAV orthophoto. Furthermore, PS points and UAV monitoring result are a severe challenge in vegetated areas. We are typed as label AN and label DN not analyzed. However, the absolute coordinate direction is easier to understand, but it's hard to transform 3D coordinate since we lack GPS station in the interested area. To obtain consistent data, LOS direction analysis is adopted. Therefore, we transform MUAV image displacement of monitoring result to the LOS direction, and then analyze the behavior between the PS point and MUAV image displacement. MUAV image and PS points have same

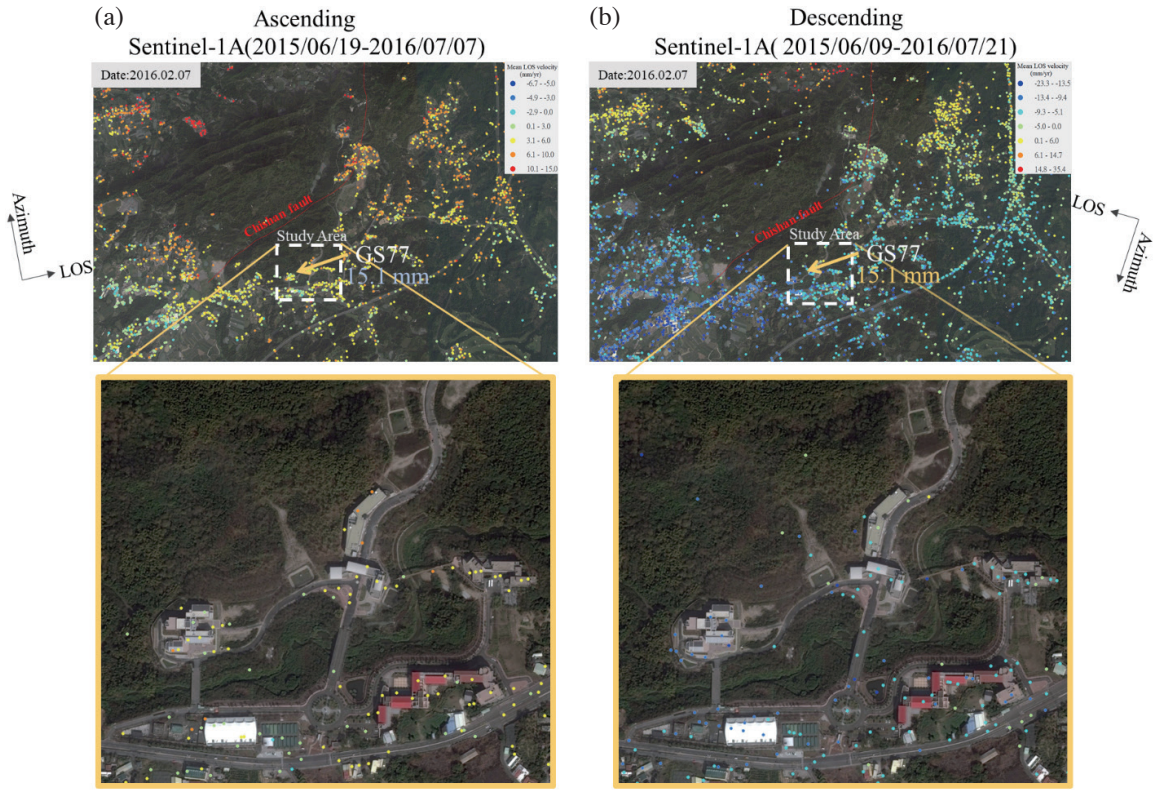

Fig. 4. Result of PS-InSAR by Sentinel-1A ascending and descending satellite radar images of Yanchao District, Kaohsiung, Taiwan. Yellow Square is the area of interest. (a) PS Points of ascending SAR images (2015/06/19 - 2016/07/07). (b) PS Points of descending SAR images (2015/06/09 - 2016/07/21).

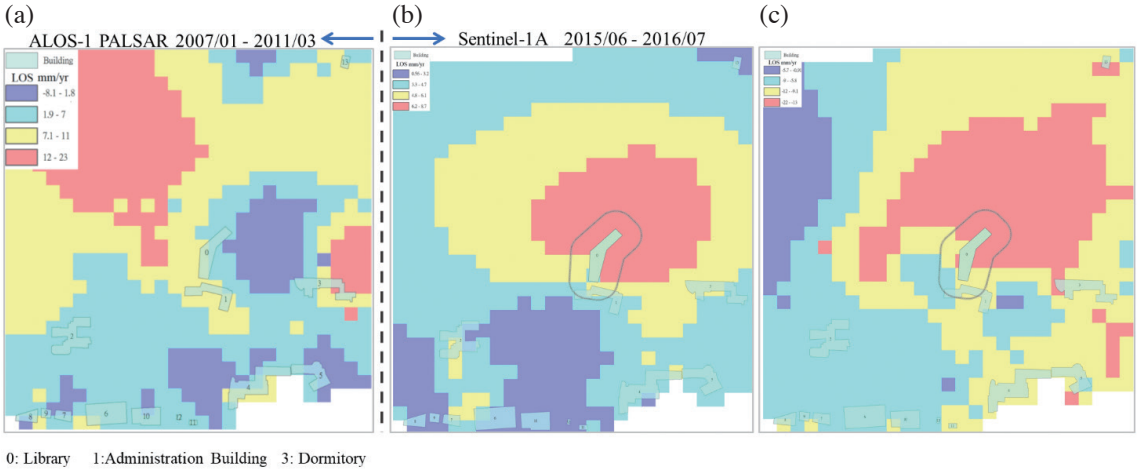

Fig. 5. Results using PS points to raster of deformation level classification and extract interested area near the building. (a) ALOS-1 PALSAR result showed maximum deformation region as label 3 (Dormitory). (b) Sentinel-1 A of ascending result showed maximum deformation region as label 0 (Library). (c) Sentinel-1 A of descending result shown maximum deformation region as 0 (Library).

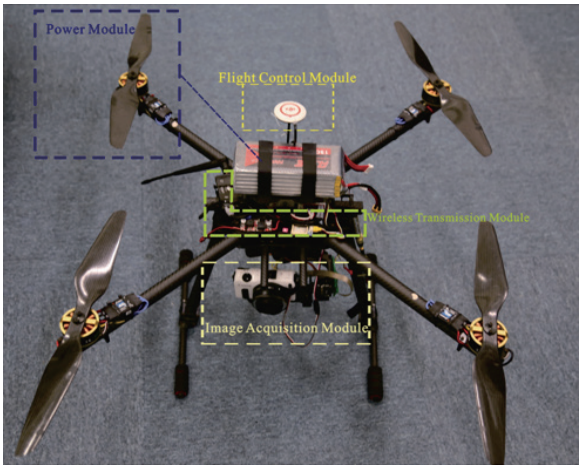

Fig. 6. Photographs of the self-made 4-rotor MUAV platform.

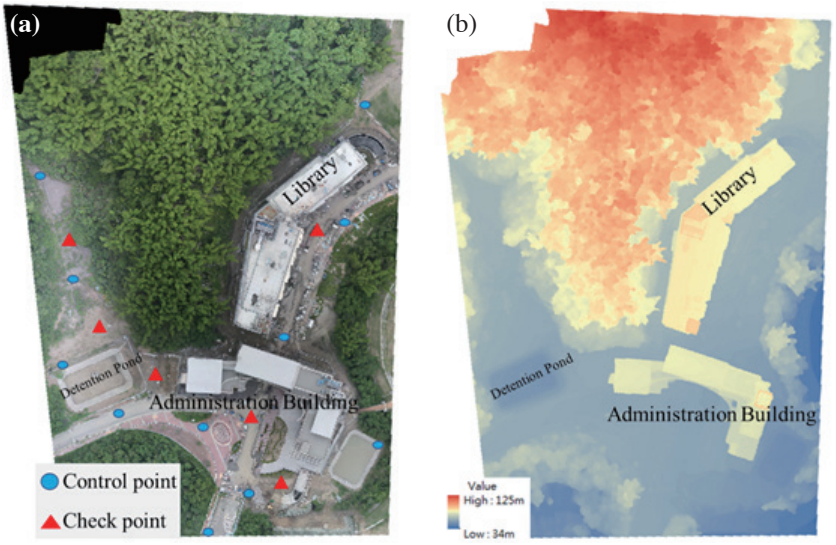

Fig. 7. Orthophoto and DSM of interested area on 2015/06 (a) 2015/06 orthophoto and (b) 2015/06 DSM.

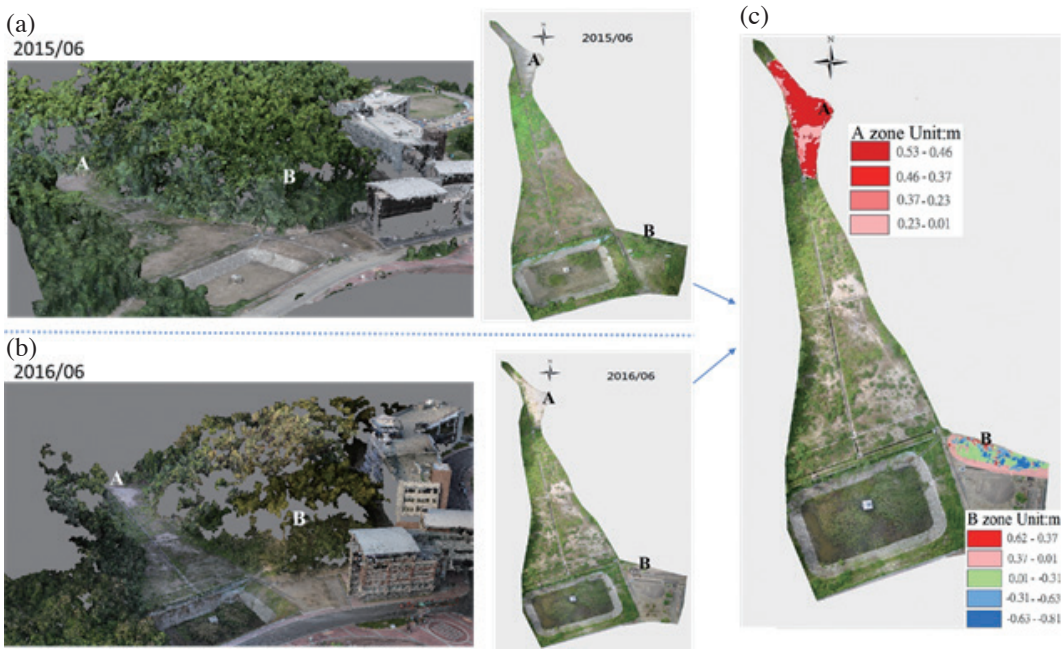

Fig. 8. 3D point cloud and orthophoto of interested area on 2015/06 and 2016/06 (a) local 3D point cloud and orthophoto on 2015/06; (b) local 3D point cloud and orthophoto on 2016/06; and (c) deformation of interested area between 2015/06 - 2016/06.

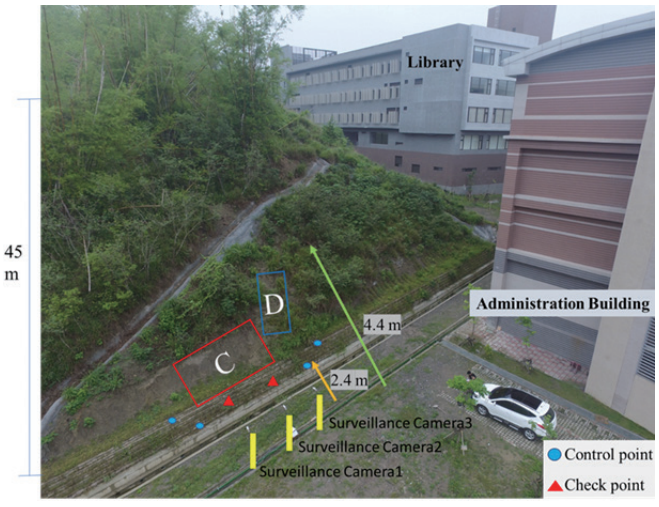

Fig. 9. High-risk zone and positions of cameras.

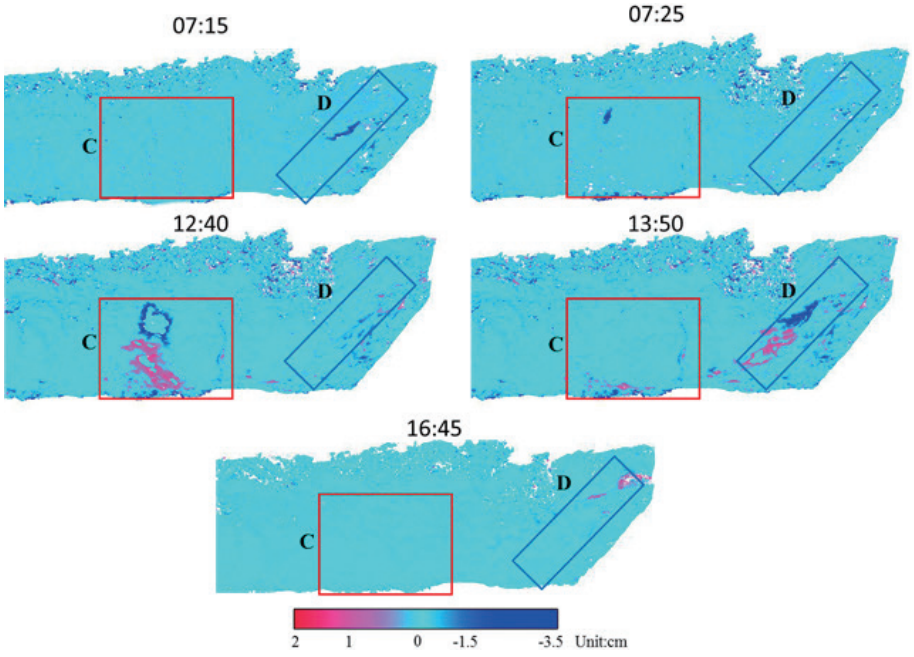

Fig. 10. Surface deformation monitoring from a real-time surveillance camera system in high-risk region. The deformation started at 7:15 for Area D; and it occurred at 7:25 on Area C. The biggest deformation of Area C appeared at 12:40; and it occurred at 13:50 on Area D. The whole high-risk region stops changing at 16:45. Blue represents the erosion area and red is the deposition area.

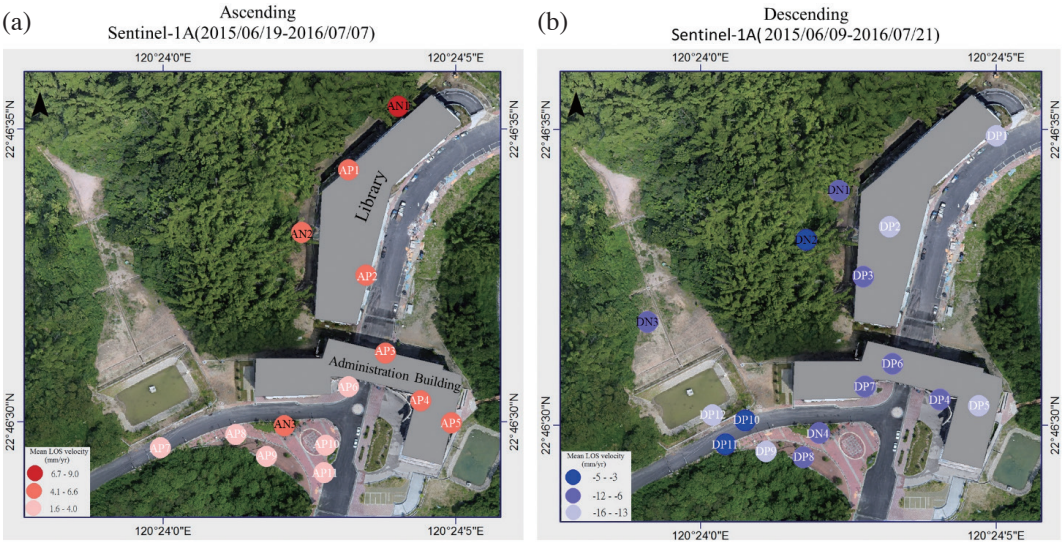

Fig. 11. PS point and MUAV orthophoto image overlay (blue and red points are the PS point of the Sentinel-1A radar satellite image, P points are located at the point of buildings and road, and N points are located in the vegetation area).

date during 2015/06 to 2016/06 (Fig. 12). The PS points on buildings and ground are then selected.

In Fig. 12a, we choose P1-P6 positions in buildings area that indicate more PS than MUAV displacement, and choose P7-P11 on road that show more MUAV image than PS displacement. For SAR image result of descending analysis in Fig. 12b, we choose P1 - P7 positions in buildings area. P2 - P7 seem reasonable for same construction region but P1 appears to be clearly different because the point is located at the junction of the building and ground, limiting the elevation interpolation process of the MUAV image. On the other hand, P8 - P12 point area on road looks unstable and may be due to the junction of the hillslope and the retaining wall. Both results show acceleration in the same time.

To further analyze surface deformation by two different remote-sensing techniques, our analyses result (Fig. 12) indicate that the two techniques used to obtain the deformation trend is quite consistent, which gives deformation trends despite the few number of points. The difference of both techniques is about 5 mm, especially at buildings and roads region. It is important to note that due to construction of buildings and roads, same trends will be visible. Therefore, hierarchical monitoring in investigating a large region can be considered as an effective work, which gives a reasonable interested area by PS-InSAR. The PS points result (Fig. 12) showed that the ground exhibits more displacement than the building with a ground maximum displacement of 30 mm yr^{-1} (LOS velocity). The slow displacement of the building is limited by the foundation. In addition, MUAV image can be utilized to obtain more details in interested area.

5.2 Real-Time Surveillance Cameras Monitoring

From Fig. 9, the high-risk region can be separated into C and D zones. A rainfall event on 2017/06/04 is then experienced and a real-time monitoring system is adopted to observe the entire region, obtaining a total deformation data (Fig. 13). Figure 13 shows the blue and red zones corresponding to erosion zone (C-1, D-1) and deposed zone (C-2, D-2), respectively.

To further analyze deformation behavior, the point cloud to point cloud displacements in each period were calculated by the Hausdorff distance method (Huttenlocher et al. 1992). Final calculated results shown in Fig. 14. C and D zone have experienced erosion and deposition phenomenon. In Fig. 14, the C-1 zone appeared as an arc shape with a maximum depth of surface erosion of 19.0 cm. The soil stacks maximum height in C-2 zone is 14.0 cm. The D-1 zone exhibits gradual erosion in time without clear displacement behavior. D-2 zone has less deposition with a maximum height of 9.0 cm. The result depicts more C zone than D zone displacement. Moreover, C zone exhibits a high-rate displacement of 0.75 cm h^{-1}. Furthermore, actual scenario finds the crack at upper D zone. Therefore, we can consider C zone as a highly sensitive position. Monitoring must be kept to prevent the hillslope from severe disaster.

The high-risk region was selected from the hierarchical monitoring result. This confirms that our study provided an effective hierarchical monitoring procedure around buildings in a wide hillslope area.

6. CONCLUSION

In this paper, the monitoring procedure results describing the NKUST Yanchao campus deformation condition have been observed, which were achieved by different remote-sensing techniques characteristic monitoring different regions. The study area exhibits a wide range and consists of many hillslopes and mudstone condition that can cause damage to buildings. Thus, deformation on the area needs to be monitored. However, variations in deformation can be due to different applicability in different remote-sensing techniques, as well as the difference in the time period studied at each case. Therefore, different remote-sensing techniques are adopted to create hierarchical monitoring procedure. First, PS-InSAR method investigates displacement in the wide area where a serious deformation area is selected at around the buildings and becomes an interested area according to Fig. 5. Results then show the MUAV-collect images at the interested area under an approximate time, which evaluates the high-risk region (Fig. 8). Finally, high-risk regions used real-time surveillance cameras to focus (Fig. 9).

Based on the experiment discussed, PS-InSAR and MUAV image achieve similar displacement trends at buildings and roads region over the interested area, thus large region investigation can be considered reliable and reasonable, which provides MUAV flight area effective reference. Furthermore, surveillance cameras' advantages include obtaining real-time displacement, providing clear surface erosion behavior when user is without at actual scenes (Fig. 14), and launching prevention when facing disaster immediately. Therefore, we have experimentally demonstrated that integrating images of three different techniques is a reliable monitoring procedure. Indeed, the study area finds clear deformation and a maximum movement rate of 0.75 cm h^{-1} around the building, which achieve the provided hierarchical monitoring procedure, proving to be an efficient method of hillslopes monitor.

Acknowledgements The appreciation belongs to National Kaohsiung University of Science and Technology for supporting us system equipment funds.

REFERENCES

Akca, D., 2013: Photogrammetric monitoring of an artificially generated shallow landslide. *The Photogrammetric*

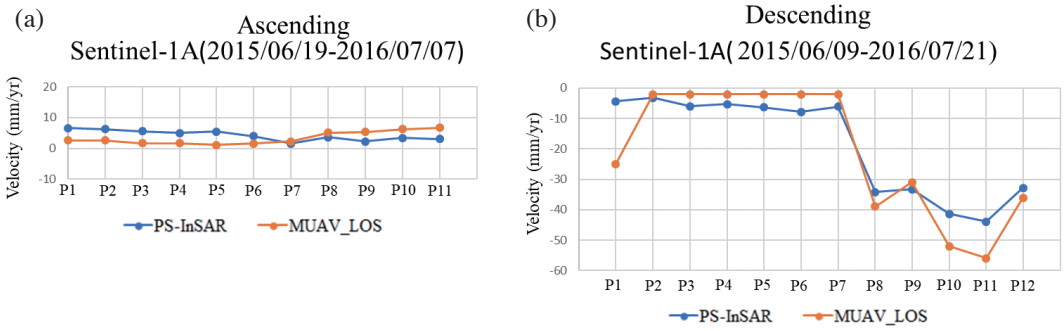

Fig. 12. Comparison of the PS points and MUAV image LOS deformation.

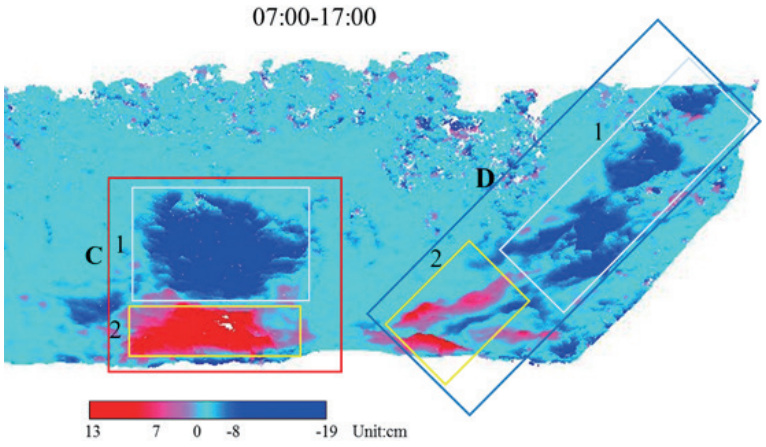

Fig. 13. Surface deformation analysis of the C and D zones in the high-risk region.

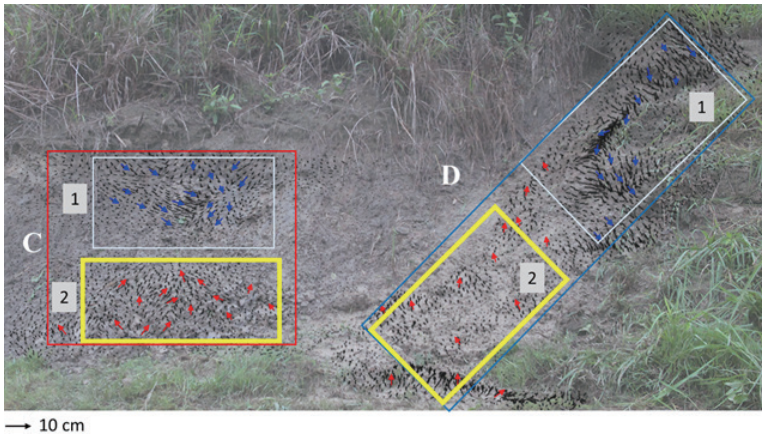

Fig. 14. Image of the high-risk regions C and D (C-1 and D-1 is the erosion area, C-2, D-2 is the deposed area.) the point cloud to point cloud displacements were calculated by the Hausdorff distance method.

Record, **28**, 178-195, doi: 10.1111/phor.12016. [Link]

Berti, M., A. Corsini, S. Franceschini, and J. P. Iannacone, 2013: Automated classification of Persistent Scatterers Interferometry time series. *Nat. Hazards Earth Syst. Sci.*, **13**, 1945-1958, doi: 10.5194/nhess-13-1945-2013. [Link]

Carvajal, F., F. Agüera, and M. Pérez, 2011: Surveying a landslide in a road embankment using unmanned aerial vehicle photogrammetry. *Int. Arch. Photogramm. Remote Sens. Spatial Inf. Sci.*, **XXXVIII-1/C22**, 201-206, doi: 10.5194/isprsarchives-XXXVIII-1-C22-201-2011. [Link]

Central Weather Bureau of Taiwan, 2020: Monthly Mean, Mean Temperature. Available at https://www.cwb.gov.tw/V8/C/C/Statistics/monthlymean.html.

Chang, C.-M., 2018: Toward Connecting Failure Mechanism - Investigation of Precipitation Induced Mudstone Landsliding. Master Thesis, Department of Civil Engineering, National Cheng Kung University, Tainan City, Taiwan, 74 pp. (in Chinese)

Ching, K.-E., J. R. Gourley, Y.-H. Lee, S.-C. Hsu, K.-H. Chen, and C.-L. Chen, 2016: Rapid deformation rates due to development of diapiric anticline in southwestern Taiwan from geodetic observations. *Tectonophysics*, **692**, 241-251, doi: 10.1016/j.tecto.2015.07.020. [Link]

Colesanti, C., A. Ferretti, C. Prati, and F. Rocca, 2003: Monitoring landslides and tectonic motions with the Permanent Scatterers Technique. *Eng. Geol.*, **68**, 3-14, doi: 10.1016/S0013-7952(02)00195-3. [Link]

Cook, K. L., 2017: An evaluation of the effectiveness of low-cost UAVs and structure from motion for geomorphic change detection. *Geomorphology*, **278**, 195-208, doi: 10.1016/j.geomorph.2016.11.009. [Link]

Crosetto, M., O. Monserrat, M. Cuevas-González, N. Devanthéry, and B. Crippa, 2016: Persistent Scatterer Interferometry: A review. *ISPRS J. Photogram. Rem. Sens.*, **115**, 78-89, doi: 10.1016/j.isprsjprs.2015.10.011. [Link]

Deffontaines, B., K.-J. Chang, J. Champenois, B. Fruneau, E. Pathier, J.-C. Hu, S.-T. Lu, and Y.-C. Liu, 2017: Active interseismic shallow deformation of the Pingting terraces (Longitudinal Valley – Eastern Taiwan) from UAV high-resolution topographic data combined with InSAR time series. *Geomatics, Natural Hazards and Risk*, **8**, 120-136, doi: 10.1080/19475705.2016.1181678. [Link]

Deffontaines, B., K.-J. Chang, J. Champenois, K.-C. Lin, C.-T. Lee, R.-F. Chen, J.-C. Hu, and S. Magalhaes, 2018: Active tectonics of the onshore Hengchun Fault using UAS DSM combined with ALOS PS-InSAR time series (Southern Taiwan). *Nat. Hazards Earth Syst. Sci.*, **18**, 829-845, doi: 10.5194/nhess-18-829-2018. [Link]

Du, Y., Q. Xu, L. Zhang, G. Feng, Z. Li, R.-F. Chen, and C.-W. Lin, 2017: Recent Landslide Movement in Tsaoling, Taiwan Tracked by TerraSAR-X/TanDEM-X DEM Time Series. *Remote Sens.*, **9**, 353, doi: 10.3390/rs9040353. [Link]

Fernández, T., J. L. Pérez, F. J. Cardenal, A. López, J. M. Gómez, C. Colomo, J. Delgado, and M. Sánchez, 2015: Use of a light UAV and photogrammetric techniques to study the evolution of a landslide in Jaén (southern Spain). *Int. Arch. Photogramm. Remote Sens. Spatial Inf. Sci.*, **XL-3/W3**, 241-248, doi: 10.5194/isprsarchives-XL-3-W3-241-2015. [Link]

Fernández, T., J. Pérez, J. Cardenal, J. Gómez, C. Colomo, and J. Delgado, 2016: Analysis of landslide evolution affecting olive groves using UAV and photogrammetric techniques. *Remote Sens.*, **8**, 837, doi: 10.3390/rs8100837. [Link]

Ferretti, A., C. Prati, and F. Rocca, 2000: Nonlinear subsidence rate estimation using permanent scatterers in differential SAR interferometry. *IEEE Trans. Geosci. Remote Sensing*, **38**, 2202-2212, doi: 10.1109/36.868878. [Link]

Ferretti, A., C. Prati, and F. Rocca, 2001: Permanent scatterers in SAR interferometry. *IEEE Trans. Geosci. Remote Sensing*, **39**, 8-20, doi: 10.1109/36.898661. [Link]

Hilley, G. E., R. Bürgmann, A. Ferretti, F. Novali, and F. Rocca, 2004: Dynamics of Slow-Moving Landslides from Permanent Scatterer Analysis. *Science*, **304**, 1952-1955, doi: 10.1126/science.1098821. [Link]

Hooper, A., H. Zebker, P. Segall, and B. Kampes, 2004: A New Method for Measuring Deformation on Volcanoes and Other Natural Terrains Using InSAR Persistent Scatterers. *Geophys. Res. Lett.*, **31**, doi: 10.1029/2004GL021737. [Link]

Hooper, A., P. Segall, and H. Zebker, 2007: Persistent scatterer interferometric synthetic aperture radar for crustal deformation analysis, with application to Volcán Alcedo, Galápagos. *J. Geophys. Res.*, **112**, doi: 10.1029/2006JB004763. [Link]

Hsieh, Y.-C., Y.-C. Chan, and J.-C. Hu, 2016: Digital elevation model differencing and error estimation from multiple sources: A case study from the Meiyuan Shan landslide in Taiwan. *Remote Sens.*, **8**, 199, doi: 10.3390/rs8030199. [Link]

Huang, M.-H., R. Bürgmann, and J.-C. Hu, 2016a: Fifteen years of surface deformation in Western Taiwan: Insight from SAR interferometry. *Tectonophysics*, **692**, 252-264, doi: 10.1016/j.tecto.2016.02.021. [Link]

Huang, M.-H., H. Tung, E. J. Fielding, H.-H. Huang, C. Liang, C. Huang, and J.-C. Hu, 2016b: Multiple fault slip triggered above the 2016 M_w 6.4 MeiNong earthquake in Taiwan. *Geophys. Res. Lett.*, **43**, 7459-7467, doi:

10.1002/2016GL069351. [Link]

Huttenlocher, D. P., W. J. Rucklidge, and G. A. Klanderman, 1992: Comparing images using the Hausdorff distance under translation. Proceedings 1992 IEEE Computer Society Conference on Computer Vision and Pattern Recognition, Champaign, IL, USA, 654-656, doi: 10.1109/CVPR.1992.223209. [Link]

Ide, R. and H. Oguma, 2013: A cost-effective monitoring method using digital time-lapse cameras for detecting temporal and spatial variations of snowmelt and vegetation phenology in alpine ecosystems. *Ecol. Informat.*, **16**, 25-34, doi: 10.1016/j.ecoinf.2013.04.003. [Link]

James, M. R. and S. Robson, 2012: Straightforward reconstruction of 3D surfaces and topography with a camera: Accuracy and geoscience application. *J. Geophys. Res.*, **117**, doi: 10.1029/2011JF002289. [Link]

Jenks, G. F., 1963: Generalization in statistical mapping. *Ann. Assoc. Am. Geogr.*, **53**, 15-26, doi: 10.1111/j.1467-8306.1963.tb00429.x. [Link]

Lillesand, T., R. W. Kiefer, and J. Chipman, 2008: Remote Sensing and Image Interpretation, Wiley, 756 pp.

Lin, D.-Y., G.-Y. Gong, and C.-S. Hsieh, 2017: The study of Real-Time dynamics of monitoring slope by Multi-Camera. The Taiwan Geographic Information Society Annual Meeting & Academic Conference, National Taipei University, Taiwan, 56-62.

Lu, H.-W., 2014: Investigating the Safety of the Mudstone Slopes Sited on the Shenshuei Area in Kaohsiung City. Master Thesis, National Kaohsiung University of Science and Technology, Kaohsiung City, Taiwan, 80 pp. (in Chinese)

Mancini, F., M. Dubbini, M. Gattelli, F. Stecchi, S. Fabbri, and G. Gabbianelli, 2013: Using unmanned aerial vehicles (UAV) for high-resolution reconstruction of topography: The structure from motion approach on coastal environments. *Remote Sens.*, **5**, 6880-6898, doi: 10.3390/rs5126880. [Link]

Nadim, F., O. Kjekstad, P. Peduzzi, C. Herold, and C. Jaedicke, 2006: Global landslide and avalanche hotspots. *Landslides*, **3**, 159-173, doi: 10.1007/s10346-006-0036-1. [Link]

National Kaohsiung University of Science and Technology (NKUST), 2009: Report of Geologic drilling and test analysis report in YanChao campus of NKUST. (in Chinese)

Niethammer, U., S. Rothmund, M. R. James, J. Travelletti, and M. Joswig, 2010: UAV-based remote sensing of landslides. *Int. Arch. Photogramm. Remote Sens. Spatial Inf. Sci.*, **XXXVIII**, 496-501.

Niethammer, U., S. Rothmund, U. Schwaderer, J. Zeman, and M. Joswig, 2011: Open source image-processing tools for low-cost UAV-based landslide investigations. *Int. Arch. Photogramm. Remote Sens. Spatial Inf. Sci.*, **XXXVIII-1/C22**, 161-166, doi: 10.5194/isprsarchives-XXXVIII-1-C22-161-2011. [Link]

Niethammer, U., M. R. James, S. Rothmund, J. Travelletti, and M. Joswig, 2012: UAV-based remote sensing of the Super-Sauze landslide: Evaluation and results. *Eng. Geol.*, **128**, 2-11, doi: 10.1016/j.enggeo.2011.03.012. [Link]

Peck, R. B., 1969: Deep excavations and tunneling in soft ground. Proceedings of the 7th International Conference on Soil Mechanics and Foundation Engineering, Mexico City, 225-290.

Pesci, A., G. Teza, G. Casula, F. Loddo, P. De Martino, M. Dolce, F. Obrizzo, and F. Pingue, 2011: Multitemporal laser scanner-based observation of the Mt. Vesuvius crater: Characterization of overall geometry and recognition of landslide events. *ISPRS J. Photogram. Rem. Sens.*, **66**, 327-336, doi: 10.1016/j.isprsjprs.2010.12.002. [Link]

Righini, G., V. Pancioli, and N. Casagli, 2012: Updating landslide inventory maps using Persistent Scatterer Interferometry (PSI). *Int. J. Remote Sens.*, **33**, 2068-2096, doi: 10.1080/01431161.2011.605087. [Link]

Shih, P. T-Y., H. Wang, K.-W. Li, J.-J. Liao, and Y.-W. Pan, 2019: Landslide monitoring with interferometric SAR in Liugui, a vegetated area. *Terr. Atmos. Ocean. Sci.*, **30**, 521-530, doi: 10.3319/TAO.2019.04.13.01. [Link]

Stumpf, A., J.-P. Malet, N. Kerle, U. Niethammer, and S. Rothmund, 2013: Image-based mapping of surface fissures for the investigation of landslide dynamics. *Geomorphology*, **186**, 12-27, doi: 10.1016/j.geomorph.2012.12.010. [Link]

Turner, D., A. Lucieer, and S. de Jong, 2015: Time series analysis of landslide dynamics using an unmanned aerial vehicle (UAV). *Remote Sens.*, **7**, 1736-1757, doi: 10.3390/rs70201736. [Link]

Vasuki, Y., E.-J. Holden, P. Kovesi, and S. Micklethwaite, 2014: Semi-automatic mapping of geological Structures using UAV-based photogrammetric data: An image analysis approach. *Comput. Geosci.*, **69**, 22-32, doi: 10.1016/j.cageo.2014.04.012. [Link]